Supplementary Information (SI) for Journal of Materials Chemistry C.
This journal is © The Royal Society of Chemistry 2025

Electronic Supplementary Information (ESI)

Temperature dependent trion induced tunability of the terahertz signal response enabled by intraband transitions in monolayer WS_2

Saloni Sharma,[a,b,c] Divyansh Pratap Singh,[a] Shreeya Rane,[d] Jishnu Murukeshan,[c] Tymofii S. Pieshkov, [c,e] Shubhda Srivastava,[a] Soumyabrata Roy,[c] Anand B Puthirath,[c] Guanhui Gao,[f,g] Ruturaj Puranik,[h] Utkarsh Pandey,[h] Snehal Haldankar,[h] Vibhavari Parkar,[h] Fathimath Faseela, [h] Shriganesh S. Prabhu, [h] Dibakar Roy Chowdhury,[d] P M Ajayan,*[c] and Bipin Kumar Gupta*[a,b]

[a.] *Photonic Materials Metrology Sub Division, Advanced Materials and Device Metrology Division, CSIR-National Physical Laboratory, Dr. K. S. Krishnan Road, New Delhi-110012, India*

[b.] *Academy of Scientific and Innovative Research (AcSIR), Ghaziabad-201002, India*

[c.] *Department of Materials Science and NanoEngineering, Rice University, 6100 Main Street, Houston, Texas 77005, United States*

[d.] *Mahindra Ecole Centrale, Jeedimetla, Hyderabad, Telangana 500043, India*
Present Address: School of Engineering, Anurag University, Ghatkesar, 500088, India

[e.] *Applied Physics graduate Program, Smalley-Curl Institute, Rice University, Tx, 77005, United States*

[f.] *Electron microscopy center, Material Science and NanoEngineering department, Rice University 6100 Main Street, Houston, Texas 77005, United States*

[g.] *Electron microscopy core, Division of Research, University of Houston 77204, United States*

[h.] *Department of Condensed Matter Physics and Materials Science, Tata Institute of Fundamental Research, Mumbai, Maharashtra 400005, India*

E-mail: bipinbhu@yahoo.com

S1. Optimization of growth process

The inside view of reaction chamber is shown in Figure S1a, where solid precursors Tungsten-tri-oxide (WO_3 >99.5% Purity, Sigma Aldrich) and sulfur (S >99.5% Purity, Sigma Aldrich) precursors are placed inside the quartz tube. The best growth conditions have been optimized considering several factors such as growth time, growth temperature, ramping rate, distance between the precursors, etc. as shown in Figure S1 b. Ceramic boat named as-B1 (of WO_3 powder) is placed in quartz tube at central zone of the furnace, while two highly resistive Si substrates have been systematically arranged facing upside down on another ceramic boat named as-B2 (of S powder) inside the quartz tube, 17 cm away from the furnace central zone, as illustrated in Figure S1a. The distance has been very critical parameter as it determines the vapour phase reaction rate and dissociated radical ratio rate for appropriate formation of monolayer. The vapour phase reaction is a two-step process: in first step, an intermediate phase of WO_{3-x} is formed, during which the oxide is sulfurized in next step as indicated by equation (1) & (2); this is followed by additional sulfurization to complete the correct substitution of sulfur for the unsaturated oxygen atoms formed during the first intermediate reaction.

$$2WO_3 + xS \rightarrow 2WO_{3-x} + xSO_2 \quad (1)$$

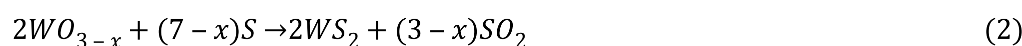

$$2WO_{3-x} + (7-x)S \rightarrow 2WS_2 + (3-x)SO_2 \quad (2)$$

To prevent additional by-products, such as multi-layer growth of WS_2, a quick cooling step must be performed once the deposition period is completed. The systematic optimized temperature profile of both precursors during the entire process has been depicted in Figure S1b. Further, several standard microscopic and spectroscopic techniques have been carried out to validate the experimental results.

The optical micrographs of APCVD grown monolayer WS_2 on Si substrate at different magnifications are shown in Figure S1c. These optical micrographs disclose intricate details about the shape of as synthesized monolayer WS_2. The optical contrast between the monolayer WS_2 and substrate provides clear visualization of layer uniformity. The morphologies of monolayer WS_2 synthesized by APCVD unveil a triangle shaped structure with a maximum lateral size of 26.26±0.16 µm as illustrated in Figure S1c.

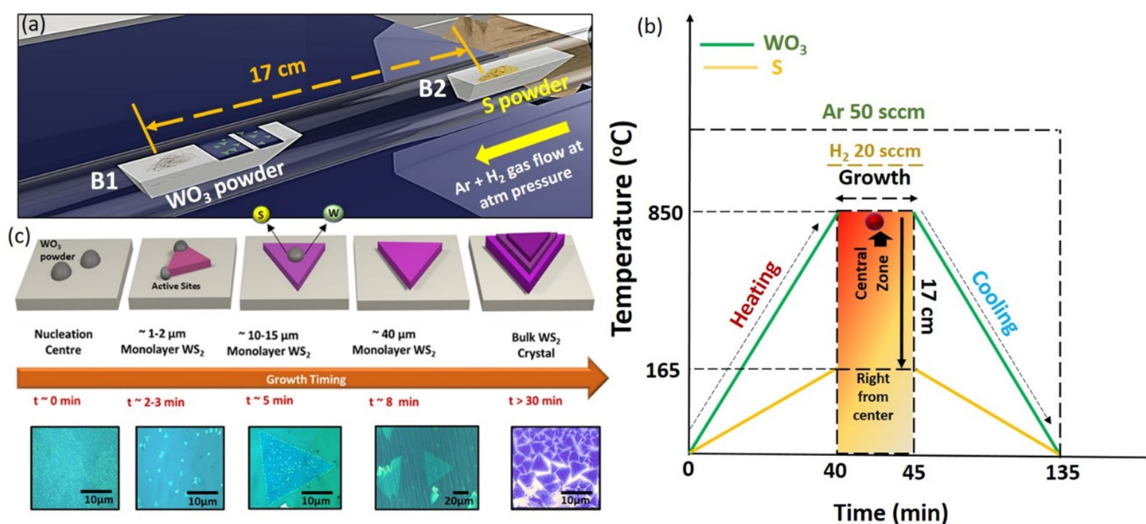

Figure 1. (a) Pictorial representation of indigenously laboratory developed APCVD setup for synthesis of monolayer WS_2, arrangement of precursors and substrate inside the furnace at central heating zone region. (b) Temperature profile of precursors inside quartz tube of horizontal split furnace, (c) systematic optimization process of growth of monolayer WS_2 and their respective optical images, scale bar is mentioned.

Table TS1. Steps of optimizing growth parameters

Distance between precursors (cm)	Precursor amount (mg)	Tempera ture (° C)	Ramping Rate (° C/min)	Growth Time (mins)	Pressure	Flow rate of H_2 (sccm)	Flow rate of Ar (sccm)	Position of substrates	No. of layers
24 cm	WO_3 ~ 15 mg S ~ 100 mg	800° C	18°C /min	5 mins	1 Atm	No H_2	350 sccm	Face down	Multi-layer
22 cm	WO_3 – 20 mg S – 20 mg	850° C	18°C/min	5 mins	1 Atm	No H_2	350 sccm	Face down	Multi-layer
21 cm	WO_3-100 mg $Na_2S_2O_3$-100mg	875°C	25° C/min	10 mins	1 Atm	No H_2	250 sccm	Face down	Multilayer
20 cm	WO_3-15.6 mg S – 103 mg	850°C	19°C/min	5 mins	1 Atm	No H_2	500 sccm	Face down	Monolayer (~1-2 µm)
17 cm	WO_3 – 50 mg S – 100 mg	870°C	25 °/min	10 mins	1 Atm	10 sccm	250 sccm	Face down	Monolayer (~ 40 µm)
17 cm	WO_3 – 50 mg S – 100 mg	870°C	25 °/min	5 mins	1 Atm	10 sccm	250 sccm	Face down	Monolayer (~ 10-20 µm)

After several statistical runs using different growth conditions, we have optimized the growth parameters for monolayer WS_2. Using the optimized growth parameters:17 cm precursor distance, 870°C growth temperature, 25°C/min ramping rate, 10 minutes growth time, and gas flows of 10 sccm H_2 and 250 sccm Ar, we successfully synthesized monolayer WS_2 films. This process was repeated 23 times under the same conditions, consistently resulting in triangular monolayer WS_2 domains ranging from 30 to 40 µm in size.

S2. Statistical areal density analysis of monolayer WS_2

SEM images are analyzed using software ImageJ and further statistical areal triangular density of monolayer WS_2 was calculated with standard procedure. Figure S2 represents the image of calculated number of synthesized monolayer WS_2 in chosen area using ImageJ software. The statistical histogram of covered monolayer WS_2 area versus the number of counts has been depicted and inset shows the

selected region for analysis, scale bar is mentioned. It is clearly evident that maximum number of monolayer WS_2 is grown in areal range 0-200 μm^2.

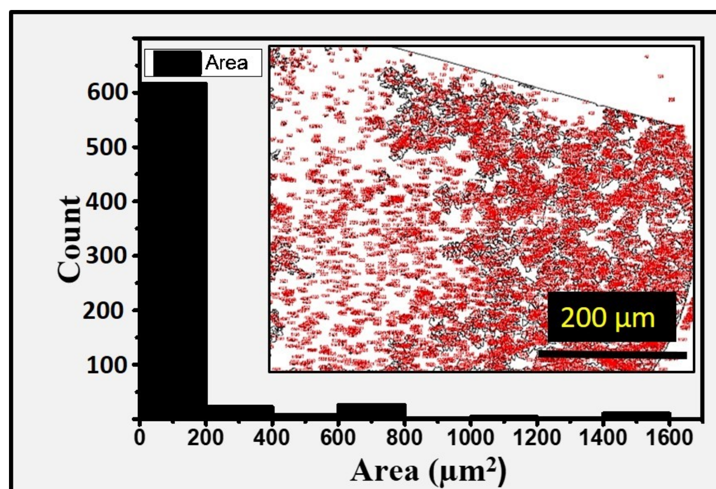

Figure 2. Statistical areal density analysis of monolayer WS_2.

S3. Transfer protocol for TEM grid

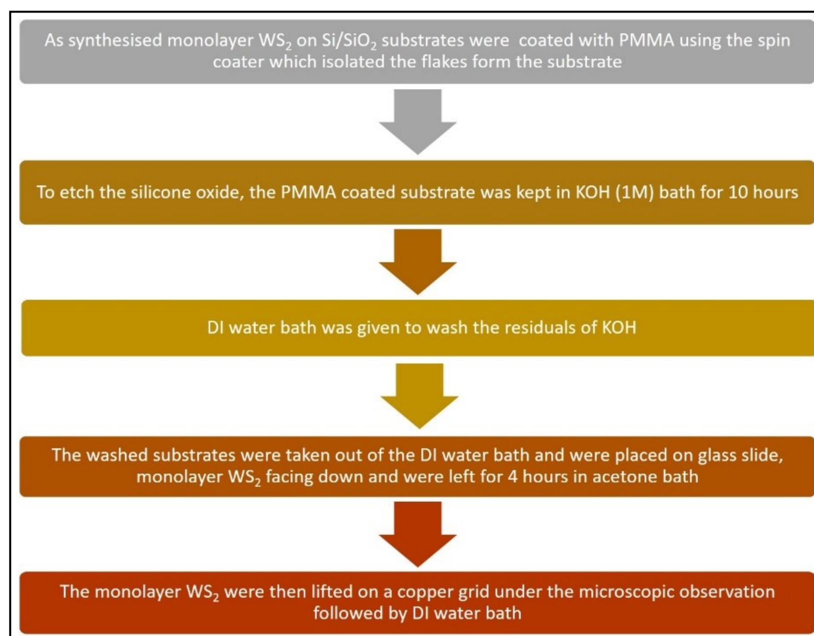

Figure 3. Transfer protocol for TEM grid.

S4. TEM characterization of monolayer WS_2

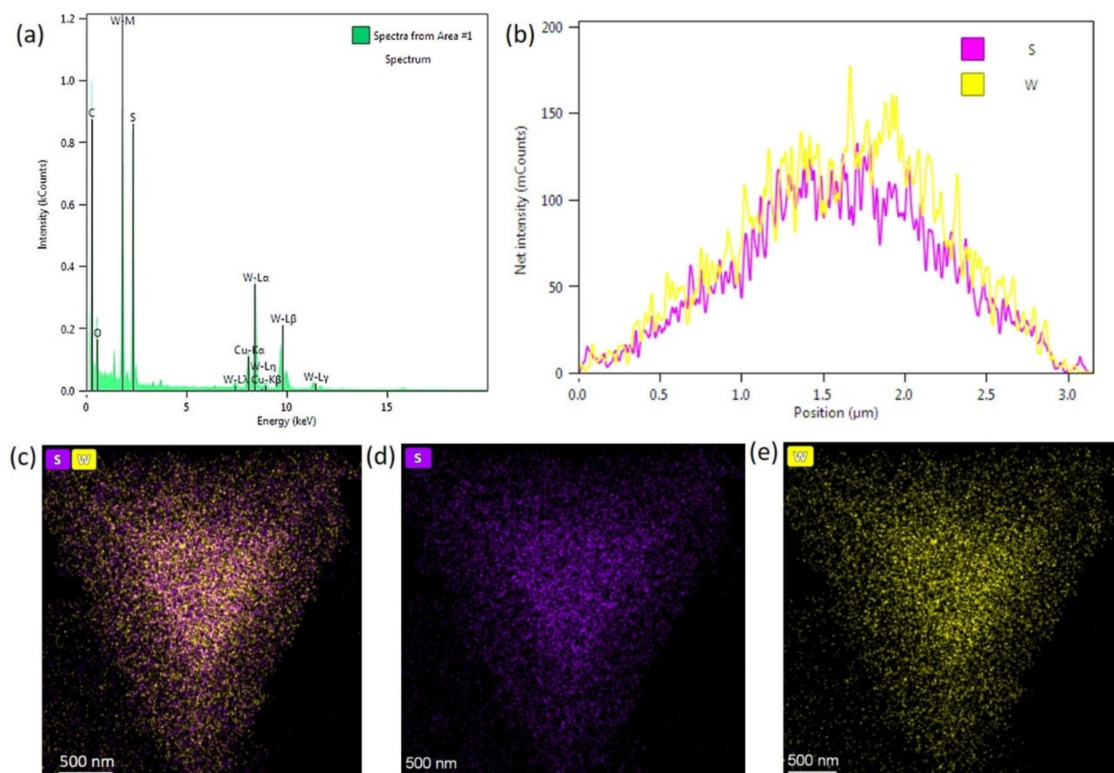

Figure 4. TEM characterization of monolayer WS_2 (a-b) Elemental scan survey of monolayer WS_2. (c-e) TEM mapping images of monolayer WS_2.

S5. XPS results

W in WS_2 may be found in a variety of oxidation states, including W^{4+} and W^{6+}, which represent various chemical environments or accountabilities. S may also exhibit variations in its coordination or oxidation state depending on the surface chemistry. The oxidation state affects an element's highest binding energy position. The typical C 1s peak (284.6 eV) is utilized as a standard reference, to rectify the shifts in respective intensities. For the W atom, two distinct XPS peaks of WS_2 has been found at binding energies of 34.7 eV, and 37.9 eV, which correspond to the $W4f_{7/2}$, and $W4f_5/_2$ core energy levels, respectively as shown in Figure 1h. The $W4f_{7/2}$, represented by 4+ valence state exhibits that sufficient sulfurization of WO_3 precursor has been consumed during the APCVD process. W in monolayer WS_2 has an electropositive characteristic that functions as an electron acceptor when it has a valence electronic configuration of $6s^25d^4$. The high-resolution XPS spectra of the S 2p doublet in the pristine WS_2 monolayers are shown in Figure 1i, confirming the successful deposition of WS_2 by APCVD technique. The S $2p_{3/2}$ and S $2p_{1/2}$ binding energies were found to be approximately 162.4 and 163.7 eV,

respectively, and were associated with the S^{2-} and S_2^{2-}species. Electronegative S^{2-} (electron donor) ions from S based vapor can effectively inject electrons into WS_2 monolayers by occupying S vacancies or being absorbed by WO_{3-x} species at the location of the vacancies.

S6. THz result analysis by Tinkham approximation

Tinkham approximation has been considered a fundamental tool in time domain terahertz data analysis for thin films, enabling us to extract optical parameters such as transmission and conductivity. The recorded spectrum in time domain further converted in frequency domain by Fast Fourier Transformation (FFT) following the equation (1).

$$E(t)\xrightarrow{FT}\frac{1}{\sqrt{2\pi}}\int_{-\infty}^{+\infty}E(t)e^{-i\omega t}dt = E(\omega) \quad (1)$$

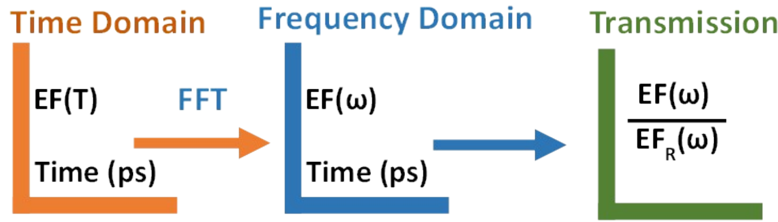

Further transmission and conductivity spectra have been obtained by using following relations:

$$T(\omega) = \frac{FFT\ (E_{sample})}{FFT(E_{substrate})} \quad (2)$$

$$\sigma(\omega) = \frac{1+n}{dZ_0}\left(\frac{1}{T(\omega)} - 1\right) \quad (3)$$

here;

FFT: Fast Fourier transformation

T (ω): Transmission

n_s: refractive index of substrate

Z_0: vacuum impedance (377 ohm)

$E_{sample}(\omega)$: THz EF signal through sample

$E_{substrate}(\omega)$: THz EF signal through bare substrate

Further the Tinkham approximation results connect by fitting experimental data to the transmittance equation. The Drude-Smith model extends the Drude model to account for carrier localization or backscattering effects with quantum confinement,

$$\sigma(\omega) = \sigma_1(\omega) + \sigma_2(\omega) \quad (4)$$

$\sigma_1(\omega)$: *represents the real part of complex conductivity*

$\sigma_2(\omega)$: *represents the complex part of complex conductivity*

$$\sigma(\omega) = \frac{e^2 n_e \tau}{m_e(1 - i\omega\tau)}\left[1 + \frac{C}{1 - i\omega\tau}\right] \quad (5)$$

e: the elementary charge,

n_e: the charge carrier concentration in monolayer WS_2,

τ : the charge carrier relaxation time.

The charge carrier concentration $n_e(T) \propto e^{-E_g/k_B T}$, relation signify the temperature dependent conductivity of monolayer WS_2.

S7. THz-TDS result analysis at different temperature by Tinkham approximation

I. **decreasing temperature (cooling):** The terahertz time-domain spectroscopy (THz-TDS) signal response was likewise documented throughout the cooling process, as depicted in Figure S5. The resulting data corroborates the findings obtained during the heating phase, thereby further validating the authenticity of the results.

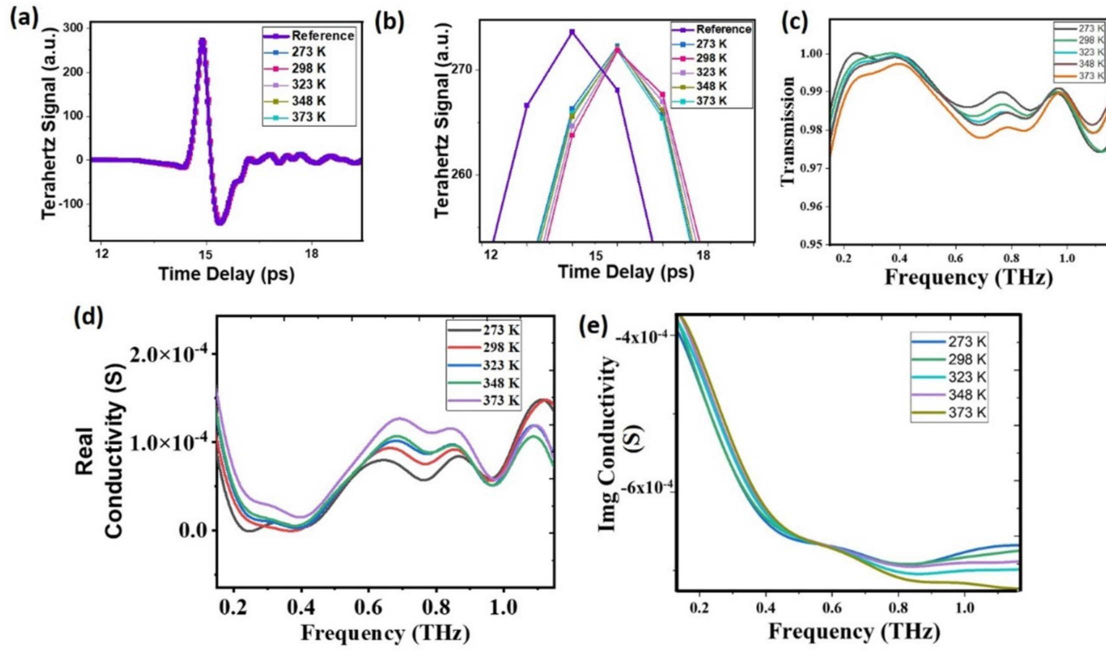

Figure 5. (a) THz signal transmitted through monolayer WS_2 on Si substrate. (b) Magnified view of transmitted THz pulse. (c) Transmitted THz amplitude through monolayer WS_2 grown on Si substrate. (d) Extracted real part of sheet conductivity of monolayer WS_2 on Si substrate in THz frequency domain. (e) Extracted imaginary part of sheet conductivity of monolayer WS_2 on Si substrate in THz frequency domain.

II. Increasing temperature (heating):

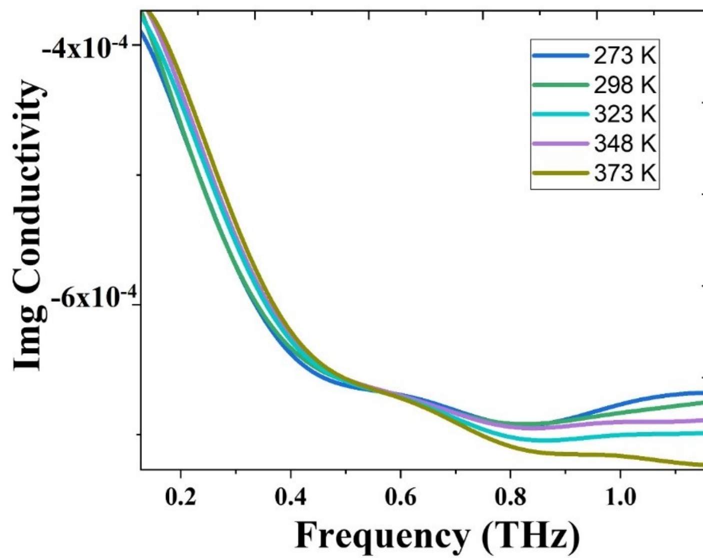

Figure 6. Extracted imaginary part of sheet conductivity of monolayer WS_2 on Si substrate in THz frequency domain.

III. Conductivity Error Analysis:

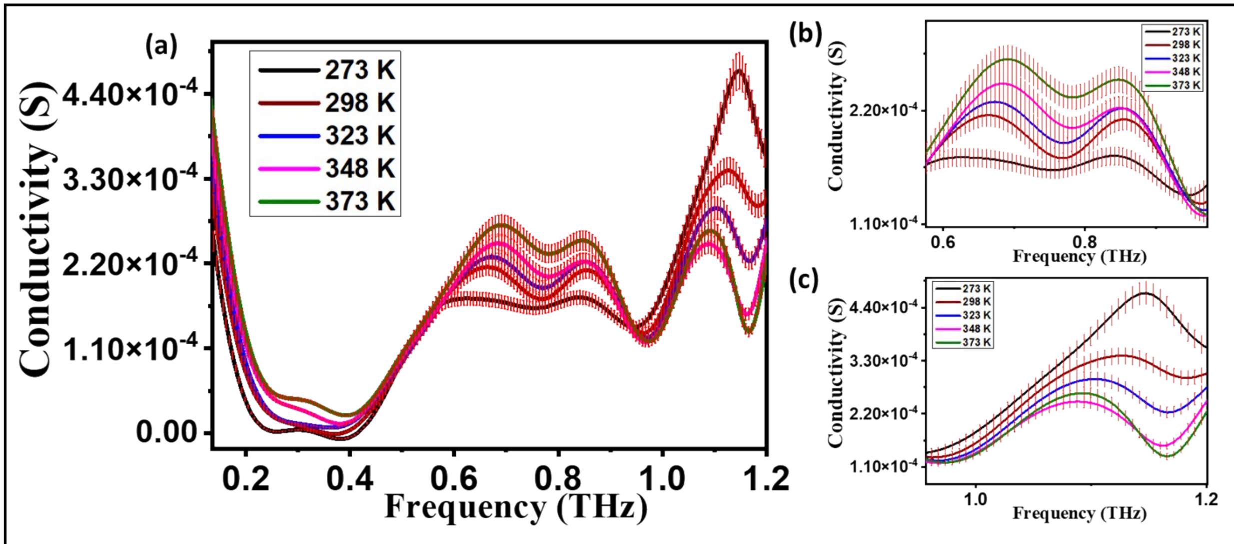

Figure 7. (a) Error analysis of conductivity spectrum at different temperatures. (b-c) enlarged view of (a) at different frequency domain.